

Radiation parametrization and clouds

Robin J. Hogan and Jonathan K. P. Shonk

*Department of Meteorology, University of Reading, United Kingdom
r.j.hogan@reading.ac.uk*

1 Introduction

The accurate parametrization of radiative transfer is of central importance to climate simulations, as well as being an important aspect to numerical weather prediction models. However, substantial errors remain in the representation of clouds, in particular the effects of their subgrid distribution on gridbox-mean fluxes and heating rates. This is a critical area requiring attention, since cloud radiative feedbacks are implicated as a leading source of uncertainty in climate prediction. This article is intended to give a broad overview of radiative transfer in the presence of clouds, from its foundations in classical electrodynamics through to recent methods for parametrizing subgrid cloud structure. It is aimed at the relative newcomer to atmospheric radiation, although hopefully radiation gurus will find it interesting as well.

We start in section 2 by showing how atmospheric optical phenomena arise from one simple process at the microscopic level, and how these phenomena may be demonstrated from numerical solutions to Maxwell's equations. We then discuss the derivation of the two-stream equations, which lie at the heart of almost all operational radiation schemes. In section 3 we show how these equations may be discretized in the presence of inhomogeneous clouds, covering both the new McICA and Tripleclouds methods. The computational resources assigned to representing the spectral variation of gaseous absorption and the spatial variation in clouds is compared. The structure of clouds may be described observationally in terms of the degree of horizontal inhomogeneity, the vertical overlap of cloud boundaries and the overlap of cloud inhomogeneities. In section 4 we review the relevant observational studies, and then in section 5 use consensus values describing cloud structure to estimate its global impact compared to the "plane-parallel" representation assumed in most current schemes. The challenge presented by 3D radiative effects is reviewed in section 6, and in section 7 we discuss some of the remaining frontiers of radiative transfer parametrization with regard to clouds.

2 From Maxwell to the two-stream equations

2.1 What is radiation?

Whether light should be thought of as particles or waves has been a matter of debate in physics for centuries. The earliest experimentally based treatise on optics was by Ibn al-Haytham (1021), who with remarkable precision proposed that light was composed of tiny particles characterized only by their energy, predating the modern concept of a photon by almost 900 years. The earliest comprehensive wave theory of light was by Huygens (1690), developing extensively the ideas of Descartes and Hooke. But with Newton (1704) holding to the particle view, it was not until Young's demonstration of optical interference patterns in the early nineteenth century that waves became the preferred model. The wave theory culminated in Maxwell's unification of electricity, magnetism and light in 1873, which also put visible light on the same footing as electromagnetic waves of other wavelengths, such as infrared radiation discovered by Herschel earlier in the century. However, the particle theory made an unexpected comeback in the early twentieth century, with Planck and Einstein demonstrating that black-body radiation and the photoelectric effect could only be explained by radiation oc-

curing in discrete packets of energy. The most complete description we now have of electromagnetic radiation is quantum electrodynamics, formulated by Feynman and others in the 1940s. In this theory the wave and particle views are reconciled (at least mathematically), in that a photon's path has a probability distribution that is determined by the interference pattern of a wave-function governed by the laws of quantum mechanics, but which nonetheless behaves similarly to a classical wave when a large number of photons are considered.

Hence, in the same way that Newtonian mechanics is a perfectly adequate approximation for representing non-relativistic geophysical fluids, so Maxwell's classical theory of electric and magnetic fields is perfectly adequate for describing the *propagation* of radiation in atmospheric applications. The one area where we do need to consider quantum effects is *emission* (and, by Kirchoff's law, absorption): here the energy and hence wavelength of emitted photons is determined by internal energy levels in the material and the Planck function, which in turn are governed by quantum mechanics. But Maxwell's equations may be used as the starting point for all other aspects of atmospheric radiative transfer.

2.2 How Maxwell's equations describe atmospheric phenomena

The incredible richness of atmospheric optics, including phenomena such as mirages, rainbows, the varied colour of the sky and the silver lining around clouds, can be shown to originate from a single process that occurs when an electromagnetic wave impinges on a dielectric material: charges in the material oscillate under the influence of the incident electric field and radiate electromagnetic waves at the same frequency. We now describe this process and demonstrate numerically how it leads to familiar optical effects.

The propagation of atmospheric radiation is governed by Maxwell's curl equations, which describe the time evolution of the electric and magnetic fields, \mathbf{E} and \mathbf{B} , and in their most fundamental form may be expressed in SI units as

$$\frac{\partial \mathbf{B}}{\partial t} = -\nabla \times \mathbf{E}; \quad (1)$$

$$\frac{\partial \mathbf{E}}{\partial t} = c^2 \nabla \times \mathbf{B} - \frac{\mathbf{J}}{\epsilon_0}, \quad (2)$$

where \mathbf{J} is the total current density (in A m^{-2}) and ϵ_0 is the permittivity of a vacuum. Here and in all subsequent equations, vectors are shown in bold. In a vacuum, the current density may be set to zero and the resulting equations can be combined to form a wave equation that supports waves of any frequency, but all of which travel with the speed of light c .

Virtually all the materials encountered by radiation in its journey through the atmosphere are poor conductors, so may be treated as *dielectrics* in the way they respond to an incident electromagnetic field. A dielectric is composed of negatively charged electrons that are "bound" to positively charged atomic nuclei. When an electromagnetic wave passes into a dielectric, a particle with charge q will feel a force given by $\mathbf{F} = q(\mathbf{E} + \mathbf{v} \times \mathbf{B})$, in addition to the forces that bind it into the atom or molecule. In practice the velocity of the bound particle \mathbf{v} is much smaller than the speed of light, so the $q\mathbf{E}$ term is dominant. Thus the positive and negative charges will be perturbed by a small amount in opposite directions, and we may assume that the amplitude of the *dipole moment* induced in each atom or molecule is proportional and parallel to the external \mathbf{E} field. Hence the sum of the dipole moments in a unit volume, the *polarization density*, may be written as $\mathbf{P} = \epsilon_0 \chi \mathbf{E}$, where χ is the dimensionless *electric susceptibility* of the material, a frequency-dependent measure of how easily it polarizes. In practice, the dipoles behave as damped simple harmonic oscillators, where the damping represents energy being transferred into thermal motions in the medium. This results in the induced polarization density not oscillating perfectly in phase with the external electric field, but lagging somewhat behind. This effect may be represented by using a complex number for χ : if we write the electric field in time-harmonic form as $\mathbf{E} = \mathbf{E}_0 e^{i\omega t}$, where ω is the angular frequency, then the induced polarization density is $\mathbf{P} = \epsilon_0 |\chi| e^{i(\omega t + \phi)}$, where the phase shift ϕ is simply the argument of the complex electric susceptibility. Since the phase shift is negative (a lag), the imaginary part of χ is negative and smaller than the real part.

The oscillating dipoles constitute an alternating electric current, with current density given by $\mathbf{J} = \partial\mathbf{P}/\partial t$. From (2) we can see that an oscillating \mathbf{J} will generate an oscillating electric field, which will in turn excite electromagnetic waves. It is this scattering on a microscopic level, and the resulting pattern of constructively and destructively interfering waves, that lead to optical effects. It turns out that the amplitude of the electric field of the scattered wave (sufficiently far away from the dipoles) is proportional to the rate of change of the current, and hence to the *acceleration* of the dipole moments, $\partial^2\mathbf{P}/\partial t^2$. The second derivative of the time-harmonic form of \mathbf{P} (above) is proportional to ω^2 . Since the power in a wave, equal to the intensity of the radiation, is proportional to the square of the wave amplitude, the intensity is proportional to ω^4 .

We represent the effect of the current by substituting $\mathbf{J} = \partial\mathbf{P}/\partial t = \varepsilon_0\chi\partial\mathbf{E}/\partial t$ into (2) to yield $\varepsilon\partial\mathbf{E}/\partial t = c^2\nabla \times \mathbf{B}$, where the *dielectric constant* (or “relative permittivity”) of the medium is defined as $\varepsilon = n^2 = \chi + 1$, and n is the familiar refractive index. But what do we do about the fact that ε may be complex? From the time-harmonic form of \mathbf{E} it may be shown that $\partial\mathbf{E}/\partial t = i\omega\mathbf{E}$. Hence, if the real and imaginary parts of the dielectric constant are $\varepsilon = \varepsilon_r - i\varepsilon_i$, then we may write

$$\frac{\partial\mathbf{E}}{\partial t} = -\frac{\varepsilon_i\omega}{\varepsilon_r}\mathbf{E} + \frac{c^2}{\varepsilon_r}\nabla \times \mathbf{B}. \quad (3)$$

Thus it can be seen that ε_i acts to attenuate the electric field, constituting absorption of energy from the wave. This makes sense, since it originates from the damping of the motion of the oscillating dipoles and transfer of this energy into heat.

We now have two equations, (1) and (3), that conveniently describe how an electromagnetic wave propagates in a dielectric. We could proceed to explore analytically the many consequences and applications of Maxwell’s equations (e.g. Chapters 18–37 of Feynman et al. 1964), but a meteorologist’s instinct is to discretize these equations and perform a numerical “forecast” of the evolution of the fields for a variety of different distributions of ε . This is known as the Finite Difference Time Domain (FDTD) method, and the most natural way to do it is on the grid devised by Yee (1966), which is staggered in both time and space. For simplicity we consider a two-dimensional solution in the x - y plane in which the electric field oscillates only in the z direction, resulting in the magnetic field only having components in the x and y directions. We define $E_{z,i,j}^n$ as the z component of \mathbf{E} at timestep n and at gridpoints i and j in the x and y directions respectively. The curl terms are most accurately discretized by placing the B_x points half way between the E_z points in the y direction, and the B_y points half way between the E_z points in the x direction. As we alternate between calculating the electric and magnetic components, it makes sense to locate them half a timestep apart. Thus, the first step is to evolve the \mathbf{B} field from the \mathbf{E} field:

$$B_{x,i,j+1/2}^{n+1/2} = B_{x,i,j+1/2}^{n-1/2} - \frac{\Delta t}{\Delta x} (E_{z,i,j+1}^n - E_{z,i,j}^n); \quad (4)$$

$$B_{y,i+1/2,j}^{n+1/2} = B_{y,i+1/2,j}^{n-1/2} - \frac{\Delta t}{\Delta x} (E_{z,i,j}^n - E_{z,i+1,j}^n), \quad (5)$$

where Δt is the timestep and Δx is the spatial resolution in both the x and y directions. The second step is to evolve the \mathbf{E} field from the \mathbf{B} field:

$$E_{z,i,j}^{n+1} = E_{z,i,j}^n \exp\left(-\frac{\varepsilon_{i,j}\omega\Delta t}{\varepsilon_{r,i,j}}\right) + \frac{c^2\Delta t}{\varepsilon_{r,i,j}\Delta x} \left(B_{y,i+1/2,j}^{n+1/2} - B_{y,i-1/2,j}^{n+1/2} - B_{x,i,j+1/2}^{n+1/2} + B_{x,i,j-1/2}^{n+1/2}\right), \quad (6)$$

where ε_i and ε_r are discretized on the same spatial grid as E_z . Plane waves can be initialized by adding a row of dipole oscillators at one side of the domain, essentially reintroducing a $-\mathbf{J}/\varepsilon_0$ term on the right-hand-side of (3). To prevent reflection from the side of the domain, it is necessary to add a few rows of absorbing material at the boundaries.

Figure 1a shows a snapshot of E_z from a simulation in which a wave initialized at the bottom of the domain propagates into a region with a left-right gradient of ε . The bending of the wave towards the region of larger ε demonstrates the process of atmospheric refraction, which is responsible for mirages (where light bends towards the larger refractive index of the colder air), and also the shimmering of light over a hot surface. Figure 1b

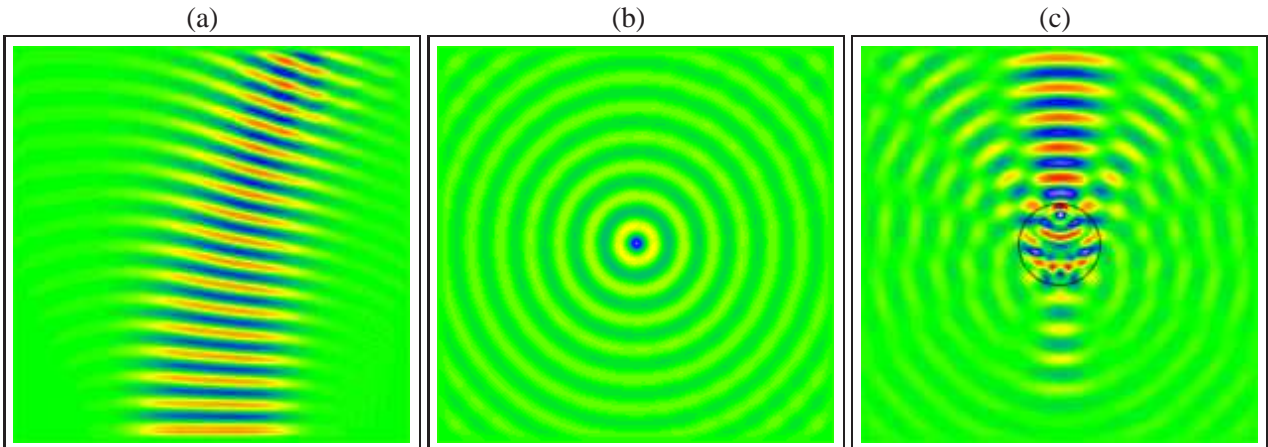


Figure 1: Instantaneous snapshots of the z -component of the electric field for 2D (x - y) simulations of an electromagnetic wave propagating into the following distributions of dielectric constant: (a) a gradient increasing from left to right, (b) a single pixel of $\epsilon = 4$ in a vacuum, and (c) a circle of $\epsilon = 4$ in a vacuum. Note that in panels (b) and (c) the field that would occur in a vacuum has been subtracted, to leave just the scattered field. Animations of these and many other cases may be found at <http://www.met.rdg.ac.uk/clouds/maxwell/>.

shows the scattered field when a wave is incident on a single dipole representing a scatterer much smaller than the wavelength; note that the scattered field is simply E_z minus the E_z that would occur without the scatterer. The result is that the dipole radiates equally in all directions. This is the same mechanism by which nitrogen and oxygen molecules in the atmosphere scatter sunlight, and the ω^4 dependence of the scattered intensity (discussed earlier) explains why the sky is blue. It should be noted that because we are performing 2D rather than 3D simulations, we have really simulated the scattering from a wire that extends infinitely in a direction perpendicular to the page, but essentially the same behaviour is observed in 3D. Figure 1c shows the same but for a scatterer larger than the wavelength, which could represent a cloud droplet or an aerosol particle. This time more of the energy is scattered forward, and the angular distribution of the scattered amplitude has much more structure. The preference for forward scattering explains why the edges of clouds illuminated from behind tend to have a “silver lining”, while the wavelength-dependent pattern of scattering in the forward direction explains the coloured corona that is often seen around the moon when it is viewed through thin clouds. An obvious example of the angular scattering pattern in the backward direction is a rainbow, which occurs for drops much larger than the wavelength.

It is remarkable that the same equations can explain such a wide variety of atmospheric phenomena when all we have changed is the spatial distribution of dielectric constant. Underlying each phenomenon is the simple process that a dielectric in the presence of an incident oscillating electric field will radiate radiation in all directions, yet the pattern of constructive and destructive interference can be completely different. Animations for a wide variety of distributions of ϵ may be found at <http://www.met.rdg.ac.uk/clouds/maxwell/>, and in addition to demonstrating scattering from different targets, they demonstrate the workings of instruments such as a diffraction grating, a Michelson interferometer, a dish antenna and a Campbell-Stokes sunshine recorder.

The FDTD method described above can be used to calculate the scattering and absorption properties for individual arbitrarily shaped particles, including the angular distribution of scattered power, and indeed it is used for light scattering by ice particles (Yang and Liou 1996). However, it can be very computationally expensive for particles large compared to the wavelength, because the grid spacing must be much smaller than the wavelength to adequately resolve the waves. Therefore more efficient time-independent methods are usually preferred; for spheres of uniform dielectric constant (such as liquid droplets), Mie (1908) provided an exact solution in terms of a series expansion. For non-spherical particles, there are a range of methods that were comprehensively reviewed by Mishchenko et al. (2000).

2.3 The radiative transfer equation

We have seen that Maxwell’s equations are sufficient to model all aspects of the propagation of atmospheric radiation, and for calculating the detailed scattering properties of individual particles. Yet they are clearly impractical for macroscale radiative transfer in the column of a General Circulation Model (GCM). It is desirable to express radiation in terms of a *radiance* $I(\Omega)$, which is the power density in direction Ω per unit frequency (or wavelength), giving it units $\text{W m}^{-2} \text{sr}^{-1} \text{Hz}^{-1}$. It was shown by Mishchenko et al. (2006) that an equation governing the relationship between radiances may be derived rigorously from Maxwell’s equations, provided that the following reasonable assumptions are made:

- Time dependence is ignored, which is valid since in the timescale of an individual photon to transit the atmosphere, atmospheric constituents can be treated as stationary and the sources of radiation (the sun in the shortwave and the surface and atmosphere in the longwave) emit continuously.
- Atmospheric particles are present in large concentrations and are randomly separated, which means that the phase difference between radiation scattered from different particles is random, and enables their intensities to be summed incoherently.
- There are no propagation effects due to the wave nature of radiation, except around individual particles. Therefore there is no diffraction around macroscale objects such as clouds and no refraction from macroscale gradients in refractive index.
- The polarization of the radiation is ignored; this is not an essential assumption, but in terms of calculating heating rates and surface fluxes, polarization is irrelevant.

The result is the monochromatic *radiative transfer equation*:

$$\Omega \cdot \nabla I(\Omega) = -\beta_e I(\Omega) + \frac{\beta_s}{4\pi} \int_{4\pi} p(\Omega', \Omega) I(\Omega') d\Omega' + S(\Omega). \quad (7)$$

The term on the left-hand-side expresses the rate of change of the radiance with distance in direction Ω . The first term on the right expresses the rate of loss by absorption or scattering, where β_e is the extinction coefficient (in m^{-1}), the reciprocal of the mean-free-path. The second term on the right expresses scattering into the direction Ω from all other directions, as governed by the scattering coefficient β_s . The scattering phase function $p(\Omega', \Omega)$ expresses the normalized fraction of energy incident in the vector direction Ω' that is scattered into direction Ω . The final term represents sources of radiation; in the longwave this is simply thermal emission by the atmosphere.

Given a 3D distribution of scattering and absorption properties, and with suitably specified boundary conditions, this equation may be solved directly. If the full 3D radiance distribution is of interest, then the leading freely available code is the Spherical Harmonics Discrete Ordinate Method (SHDOM) of Evans (1998). If integrated quantities are required [e.g. over angle to obtain irradiances (or “fluxes”), over a horizontal area to obtain domain-averaged values, or over the spectrum to obtain broad-band quantities], then the Monte Carlo method is usually more efficient.

Explicit 3D radiative transfer is not efficient enough for use in a GCM, and so the following further assumptions must be made:

- All horizontal structure is ignored, so the atmosphere varies only in height z while in the horizontal it is treated as infinite and homogeneous. Alternatively, one can picture a finite atmospheric column but with periodic boundaries so that radiation exiting one side re-enters on the other. This is known as the plane-parallel approximation.
- Radiances in all directions are represented by only two discrete directions, one into the upward hemisphere and the other into the downward hemisphere (the exact angle differs between approximations).

The exception is unscattered radiation from the sun, which is calculated separately. This is known as the two-stream approximation.

- The detailed structure of the phase function cannot be represented in the two-stream approximation, and in fact it is only necessary to characterize the phase function by a single *asymmetry factor*, defined as the average of the cosine of the scattering angles: $g = \langle \cos \theta \rangle$.

Clearly these assumptions are much less justifiable than those made in deriving (7), and ways of correcting the consequent errors are described in much of the remainder of this article. The derivation is clearly explained by Petty (2006) and results in the two-stream equations (written as one for brevity):

$$\pm \mu_1 \frac{dF^\pm}{dz} = - \left(\beta_e - \beta_s \frac{1+g}{2} \right) F^\pm + \beta_s \frac{1-g}{2} F^\mp + S^\pm. \quad (8)$$

These equations describe the interaction of the upwelling irradiance F^+ and the downwelling irradiance F^- , and have been written so that the terms can be traced easily from (7). The term on the left is prefixed by $\pm \mu_1$ in order that it represents the rate of change of flux in the direction that the radiation is travelling; μ_1 is the cosine of the angle from zenith or nadir that is regarded as “representative” of radiation travelling in all upward or downward directions. Usually a value of 0.5 or 0.6 is used, corresponding to angles of 60° or 53° (Fu et al. 1997). The first term on the right corresponds to extinction as in (7), but is reduced by a factor that accounts for scattered radiation that remains within the same hemisphere. The second term on the right corresponds to scattering from one hemisphere to the other, while the final term plays the same role as the source term in (7). It is easy to check the behaviour for different values of g : if the scattering is isotropic ($g = 0$) then half of any scattered radiation will remain in the same hemisphere and the other half will enter the other hemisphere. For a greater degree of forward scattering ($0 < g < 1$), increasingly more scattered radiation remains within the same hemisphere.

In a GCM radiation scheme, β_e may be calculated as the sum of the contributions from any liquid droplets, ice particles and aerosols that may be present in the gridbox. Its vertical integral is simply the optical depth. In general β_e is wavelength dependent, but in the case where the mean particle size is much larger than the wavelength (i.e. excluding most aerosols), geometric optics applies and we may write:

$$\beta_e = \frac{3\rho_a q_l}{2\rho_l r_{el}} + \frac{3\rho_a q_i}{2\rho_i r_{ei}}, \quad (9)$$

where q_l and q_i are the mixing ratios of liquid and ice provided by the GCM, while ρ_a , ρ_l and ρ_i are respectively the densities of the air, liquid water and solid ice. The variables r_{el} and r_{ei} are the *effective radii* of the liquid droplets and ice particles and are typically prescribed; in fact, effective radius is defined *so that* (9) holds. The asymmetry factor g and the single-scattering albedo β_s/β_e of ice and liquid are both parametrized as a function of effective radius.

It should be noted that in many applications not all of the assumptions between (7) and (8) need to be made. For example, the popular radiative transfer code “DISORT” (Stamnes et al. 1988) makes the plane-parallel assumption while fully resolving the angular radiance distribution. Likewise, Liu and Weng (2002) presented a version of the two-stream equations that retained the polarization information, for use in passive microwave remote sensing, while Hogan and Battaglia (2008) presented a time-dependent form of the two-stream equations that enabled multiple scattering from instruments such as radar and lidar to be modelled efficiently.

We have covered a lot of ground in a short time: from Maxwell’s description of microscale fluctuations in the electric and magnetic fields to the two-stream equations that are used in GCMs. Perhaps unsurprisingly, the chronology of developments in the field of radiative transfer is precisely the reverse of the order that they have been presented here. The two-stream equations were first presented by Schuster (1905) in the context of stellar atmospheres, their derivation relying on considerations of energy conservation rather than consistency with Maxwell’s equations. Interestingly, Arthur Schuster was working with Maxwell in Cambridge at the time that he published his great treatise on electromagnetism. Radiative transfer was presented in much more general

terms by Chandrasekhar (1950), and was first applied to non-uniform media by Giovanelli (1959). Yet only recently has the rigorous derivation of the radiative transfer equation (with polarization) from classical electrodynamics been made (Mishchenko 2002), putting the two-stream equations on a firmer theoretical footing.

3 Solving the two-stream equations in cloudy atmospheres

3.1 The independent column approximation

The task of a GCM radiation scheme is to provide “total” fluxes F_t^\pm (in W m^{-2}), as a function of height, that represent an average over the domain in which it is expected to act, such as the horizontal area of a grid column and the temporal duration T of a timestep (or several timesteps in the common situation that the radiation scheme is called infrequently). Since the properties of the atmosphere vary in space \mathbf{x} , time t , frequency ν , and can depend on the angle of incidence of the radiation Ω , radiances are also a function of these variables. Therefore we can think of a radiation scheme as a multi-dimensional integration over the radiance distribution:

$$F_t^\pm(z) = \frac{1}{TA} \int_T \int_A \int_\infty \int_{2\pi} I(z, \Omega, \mathbf{x}, \nu, t) \mu d\Omega d\nu d\mathbf{x} dt, \quad (10)$$

where μ is the cosine of the zenith angle consistent with direction Ω . This is actually a six-dimensional integration, since Ω represents the azimuth and elevation dependence of the radiance, and \mathbf{x} represents variations in both x and y (with A the area of a gridbox). Integration over frequency is taken to include the longwave and shortwave. The horizontal-mean heating rate due to radiation is then given by $\partial T / \partial t|_{\text{radiation}} = -(\rho_a C_p)^{-1} \partial(F_t^+ - F_t^-) / \partial z$, where C_p is the specific heat capacity of the air.

If a calculation is being performed in which the horizontal distribution of cloud properties is known, then a common approach to estimating (10) is the Independent Column Approximation (ICA), in which the continuous 3D distribution of cloud is treated as a finite number of independent columns that each behave as if they were horizontally infinite and homogeneous. An equivalent assumption made in frequency space is that there is no energy transfer between frequencies, which is much more valid (Raman scattering is the exception, but has around 10^{-5} the intensity of Rayleigh scattering). Hence integration over frequency can be performed by a discrete number of independent column calculations. If, as is common, we neglect the time dependence of the cloud field during the period T , then (10) can be represented as a double summation:

$$F_t^\pm(z) \simeq \frac{1}{N_{\mathbf{x}}} \sum_{j=1}^{N_{\mathbf{x}}} \sum_{i=1}^{N_{\nu}} F_{i,j}^\pm(z) \Delta v_i, \quad (11)$$

where $F_{i,j}^\pm$ is the flux for waveband i and spatial column j , calculated by solving the monochromatic two-stream equations given by (8). But how large should N_{ν} and $N_{\mathbf{x}}$ be for an accurate solution?

In frequency space, the very rapid variation of gaseous absorption with frequency can be treated by dividing the spectrum up into wide bands in which the solar flux (in the shortwave) or Planck function (in the longwave) is approximately constant. Within each band we perform a discrete integration not over frequency, but over absorption coefficient, taking advantage of the high degree of vertical correlation of the spectrally dependent absorption. Thus the interpretation of the summation over i in (11) is now of N_{ν} calculations for representative absorption profiles with weights Δv_i , but which do not map directly to contiguous regions of the spectrum. This is known as the correlated-k-distribution method (e.g. Lacis and Oinas 1991, Petty 2006), and the number of independent calculations used in climate models is of order one hundred. In the Rapid Radiative Transfer Model (RRTM), a version of which is now used in the ECMWF model (Morcrette et al. 2008), a total of $N_{\nu} = 252$ calculations are required in 30 bands. The Met Office uses $N_{\nu} = 115$ for climate and global forecasting applications and $N_{\nu} = 55$ for mesoscale forecasting.

In the horizontal dimension, the variability in absorption and scattering is caused not by gases but by clouds, and one would expect at least 50 columns to be necessary to represent the full distribution of cloud within a

Table 1: Comparison of the four different dimensions of integration carried out by a radiation scheme, as represented by the integrals in (10).

Dimension	Quadrature points	How well is dimension known?	Consequence of poor resolution
Time t	1/3 (e.g. every 3 h for a model with a 1-h timestep)	At the timestep of the model	Changed climate sensitivity (Morcrette 2000), poor diurnal cycle (Yang and Slingo 2001)
Angle Ω	2 (occasionally 4 for the four-stream method)	Well, except for some uncertainty on ice phase functions	$\pm 6 \text{ W m}^{-2}$ (Stephens et al. 2001)
Space \mathbf{x}	2 (clear and cloudy regions)	Poorly, due to the unknown cloud distribution	$\sim 20 \text{ W m}^{-2}$ long-term regional biases (see section 5)
Spectrum ν	100–250	Very well	Temperature biases, particularly above the tropopause (Iacono et al. 2000, Li and Barker 2005)

Table 2: Comparison of some of the properties of the variation of gaseous absorption with frequency, and the variation of cloud absorption and scattering with horizontal distance.

Gaseous absorption	Cloud absorption and scattering
Varies strongly with frequency but only a little with horizontal position due to gases being horizontally well mixed in a gridbox	Varies strongly with horizontal position and significantly with frequency
Strongly correlated in the vertical, exploited by the correlated-k-distribution method	Weakly correlated in the vertical, with the degree of correlation depending on cloud overlap discussed in section 4.2
Well known spectrum for all major gases	Exact horizontal distribution is unknown
No transfer between frequencies, except for Raman scattering which is tiny	Horizontal transfer can be significant, as discussed in section 6

gridbox, including the correlation of the cloud properties in one level with those in another. However, in typical GCMs, $N_{\mathbf{x}}$ is essentially only 2: the horizontal distribution is represented by one clear-sky region and one cloudy region in which the cloud properties are assumed to be horizontally homogenous. In fact, the clear and cloudy regions are typically not treated as two independent columns, but rather as a single column containing two regions at each level, the widths of which are dependent on the cloud fraction at that level. This is explained in more detail in section 3.4. The point to note is that, to a reasonable approximation, the computational power assigned to integration over frequency is $N_{\nu}/N_{\mathbf{x}} \sim 50$ times more than that assigned to integration in space. This is summarized in Table 1, which shows the typical number of quadrature points used for each of the four dimensions in (10). Table 2 specifically compares the frequency dependence of gaseous absorption with the spatial distribution of cloud absorption and scattering.

An obvious question arises: are we spending our computer time wisely? The accuracy–efficiency trade-off suggests “not quite”, since the bias due to using only $N_{\mathbf{x}} = 2$ is around 20 W m^{-2} in certain locations of the globe (see section 5) compared to random errors always better than 1 W m^{-1} for $N_{\nu} = 252$ (Mlawer et al. 1996). It should be pointed out that if we were to reduce N_{ν} to 2 (e.g. to have a single shortwave and a single longwave band and take no account of the spectral variation of gaseous absorption) then the associated errors would

certainly be much larger than 20 W m^{-2} , but there is nonetheless a case for increasing the spatial resolution at the expense of some of the spectral resolution. The historic reason for the much poorer spatial resolution is simply because the horizontal distribution of cloud is unknown (the GCM typically providing only cloud fraction and cloud water content) whereas the spectral distribution of gaseous absorption can be accurately calculated given the mixing ratios of the various gases.

The remainder of this document is therefore focussed on the problem of obtaining information on the spatial variation in cloud properties from observations, and how to represent this efficiently in a radiation scheme without having to reduce the resolution in the other dimensions. We have not said much about temporal or angular resolution in the integration, dimensions which are also shown in Table 1. Although it is surprising how well the two-stream approximation performs, some authors argue that sufficient accuracy is only obtained with four streams, or efficient combinations of the two- and four-stream methods (Fu et al. 1997). There is certainly a case for a more rigorous examination of the trade-offs between all four dimensions, but full consideration of the errors associated with temporal and angular discretization is beyond the scope of this article.

3.2 The Monte Carlo independent column approximation

Given the desire not to compromise on spectral resolution, there is a need to find methods to resolve the spatial variations of clouds without a significant increase in computational cost. A simple method used by Tiedtke (1996) was to scale the optical depth by a factor of 0.7, an attempt to account for the fact that inhomogeneous clouds are less reflective than their plane-parallel equivalent due to the convex relationship between albedo and optical depth. However, it has since been shown that the appropriate factor to use is a function of solar zenith angle in the shortwave (Shonk and Hogan 2008) as well as being different between the longwave and shortwave and dependent on gridbox size (Pomroy and Illingworth 2000). Therefore we require methods that have a more physical link to the distribution of water content within a gridbox.

The leading method currently is the Monte Carlo ICA (McICA), proposed by Pincus et al. (2003), which replaces the double integral in (11) by a single summation over frequency, but with the cloud profile presented to each band being a different realization of the underlying probability distribution:

$$F_i^\pm(z) \simeq \sum_{i=1}^{N_v} F_{i,j=i}^\pm(z) \Delta v_i. \quad (12)$$

Räisänen et al. (2004) developed a method for stochastically generating cloud profiles given input information on the variance of cloud water content and the degree of correlation between levels, and this is typically embedded within operational implementations of McICA. The advantage of this approach is not only that cloud structure is represented, but also that the overall efficiency is *better* than the standard method of representing clouds as horizontally homogeneous within the cloudy part of each box. The reason is that instead of N_v calls to a solver capable of representing two regions at each height (as described in section 3.4), the cloud structure can be represented by N_v calls to a simpler plane-parallel discretization of the two-stream equations (described in section 3.3). The additional cost of running the cloud generator is negligible. A possible drawback of McICA is that there is a large range of gas absorption for different parts of the spectrum (different values of i), so that even if the cloud is represented well with N_v columns, the cloud realization in each column contributes differently to the total flux, and resulting in a certain amount of “noise” compared to a full ICA calculation. However, this noise is unbiased and has been shown to have no effect on weather forecasts. The McICA is now operational in the ECMWF model (Morcrette et al. 2008). In section 3.5, an alternative method known as “Tripleclouds” is presented.

3.3 Discretizing the two stream equations

The two stream equations given by (8) describe the diffuse upwelling and downwelling fluxes in differential form, and need to be integrated over discrete layers of the atmosphere to be solved numerically. Figure 2a

This approach may be extended to more than two layers, as before, but clearly the matrix is no longer tridiagonal and so is less efficient to solve. Moreover, this treatment of cloud fraction also has a problem with accuracy when compared to the equivalent ICA calculation. Consider shortwave radiation illuminating the very simple cloud shown in Fig. 3a. As in an ICA calculation, half of the incoming solar radiation enters the cloud and half proceeds through the clear half of the column and reaches the surface (of course, a modest fraction of this will be absorbed or scattered by gases). In the ICA, radiation in the clear column that is reflected from the surface will then penetrate up through the clear air and escape (again, except for the small fraction intercepted by gases). But in our matrix solution, the downwelling fluxes would be horizontally homogenized in the single clear region beneath the cloud that such half of the radiation reflected from the surface would enter the cloud from below, and therefore be less likely to escape to space. Figure 3b compares the horizontally averaged upwelling fluxes for a two-column ICA calculation and the matrix solution (the standard two-region solver of the Edwards-Slingo code), revealing a significant bias (assuming the ICA to be correct). We refer to this as the *shadowing problem*, since it is associated with the scheme being unable to cope with the fact that part of the clear-sky region is in shadow and the other part is not. It should be stressed that because this error relates to scattering, it is much more significant in the shortwave.

One approach to tackle this problem was evident in the scheme used by Morcrette and Jakob (2000), which uses three regions, splitting the two clear regions into a part that is in the shadow of a cloud above it, and a part that has no cloud above it. Shonk and Hogan (2008) found an alternative, more computationally efficient solution. The details may be found in their paper, but essentially they appealed to the physical interpretation of how a tridiagonal system of equations is solved, and applied it to the denser matrix problem associated with more than one region at each height. In solving a tridiagonal system, the “Gaussian elimination” step involves proceeding up through the atmosphere and at each level calculating the albedo of the *entire atmosphere* below that level, as well as the total amount of radiation emitted from below that level. The “back-substitution” step then involves returning back down the atmosphere and calculating the upwelling and downwelling fluxes using these two variables. This process can be adapted to multiple regions in a way that retains much of the efficiency of the tridiagonal algorithm. In the case shown in Fig. 3a, it ensures that downwelling solar radiation in the clear-sky half of the box at an altitude of 4.5 km “sees” the albedo of the entire atmosphere below that level and is reflected back up into the same region, rather than some of it being reflected back up into the cloudy region. Figure 3b shows that the new solver based on this approach agrees almost perfectly with ICA. This new solver is now released with the Edwards-Slingo code.

3.5 The Tripleclouds approximation

Figure 2 shows that the two-stream method can be applied both in a horizontally homogeneous atmosphere, and with a division between clear and cloudy regions. However, the homogenization of the cloud within the cloudy region still results in significant biases in fluxes, by making the clouds too reflective for a given cloud water content. In reality, there is a probability density function (PDF) of optical depth (or equivalently cloud water content) across the cloudy part of a gridbox. The solution to the shadowing problem presented in the previous section enables the two-stream scheme to be efficiently extended to any number of regions horizontally, the computational cost scaling linearly with the total number of regions at all heights. But how many regions are required to represent the PDF of cloud water content? Shonk and Hogan (2008) proposed the simplest possible extension, “Tripleclouds”, in which three regions are used at each height, one clear and two cloudy. It might be expected that only two cloudy regions (one with high water content and one with low water content) would be insufficient to represent the full PDF, but the method was shown to work well using cloud-radar derived cloud fields and treating the ICA as “truth”.

Figure 4 illustrates visually what the Tripleclouds approximation means when applied to a real ice cloud observed by radar. There is some flexibility in choosing the values of the water contents to use for the two cloudy regions. If the full PDF is known then the best performance (when tested in a radiation scheme against ICA in both the shortwave and longwave) was found by

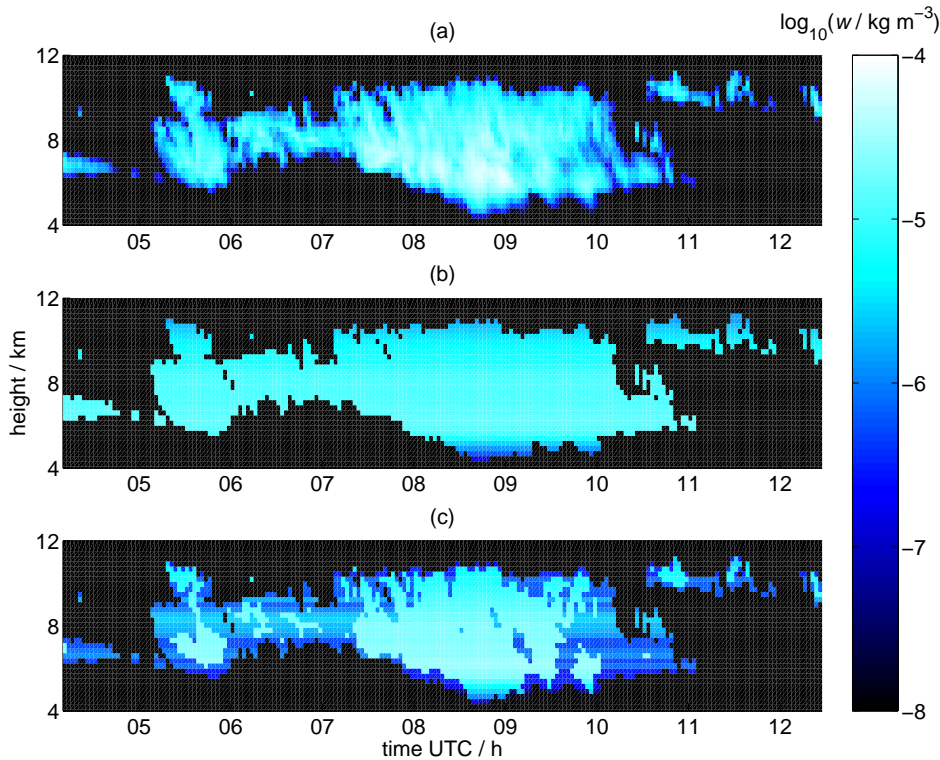


Figure 4: Comparison of the plane-parallel and Tripleclouds schemes when applied to observational data: (a) just over 8 h of radar retrievals of ice water content taken from Chilbolton, southern United Kingdom, on 28 June 2003, and the same data when (b) the plane-parallel and (c) the Tripleclouds approximations are applied directly without any parametrizations or assumptions that affect overlap. From Shonk and Hogan (2008).

- Making the cloud fractions of the two cloudy regions the same, i.e. each being half the value of the “total” cloud fraction;
- Setting the water content of the low water-content region to the 16th percentile of the full distribution;
- Setting the water content of the high water-content region to ensure that the gridbox-mean cloud water content is the same as that of the full distribution.

In an operational context the full PDF is usually not available, nor is explicit information on the overlap of the regions in one layer with the regions in another (i.e. the values to use for the overlap coefficients U and V). Some cloud schemes (e.g. Tompkins 2002, Wilson et al. 2008) prognose the variance of cloud water content, which could be used as input to Tripleclouds (or indeed McICA), but there is a need to quantify the amount of inhomogeneity that occurs in real clouds, and the degree to which they are overlapped.

4 Observations of cloud structure

This section provides a review of the available measurements of cloud inhomogeneity and cloud overlap, to provide the necessary inputs for new radiation schemes (such as McICA and Tripleclouds) to represent cloud structure globally.

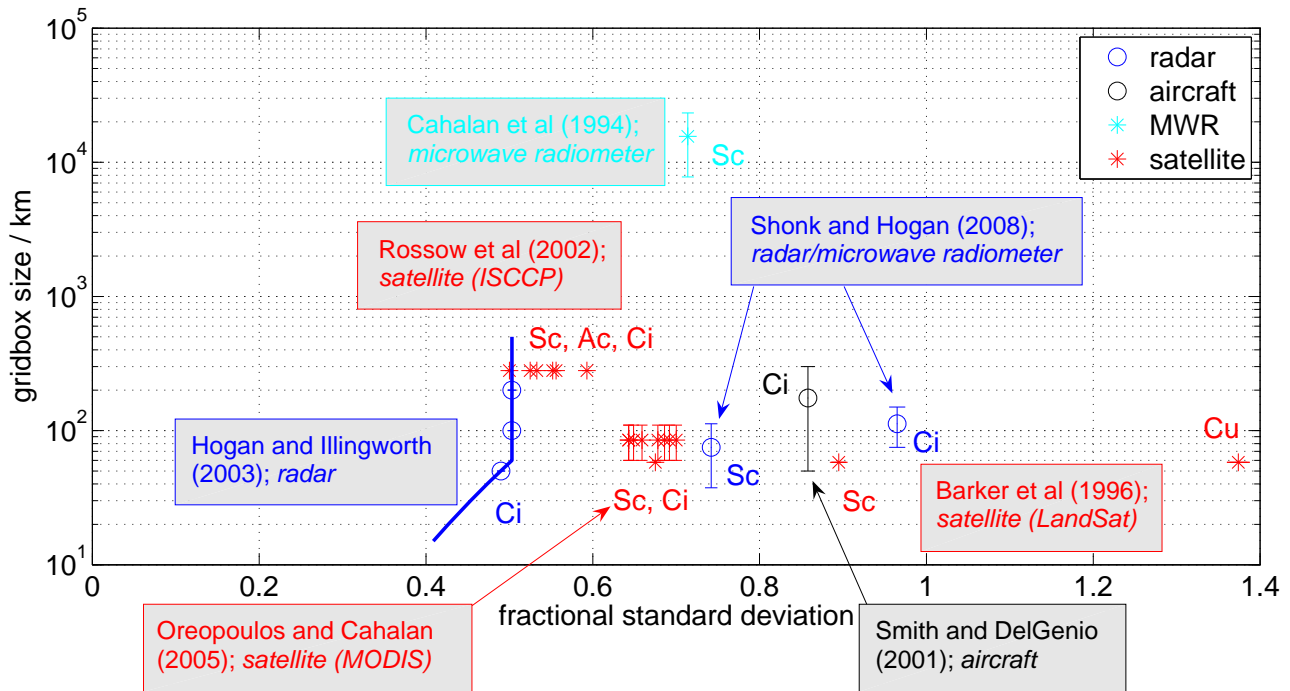


Figure 5: Summary of the values of water content fractional standard deviation found in the literature, versus the horizontal scale of the measurements. The observations are colour coded according to the instrument type, and the cloud type is shown next to the symbol. Where there is uncertainty over the gridbox size (e.g. because the samples were taken over fixed periods in time rather than space), an error bar is shown. Adapted from Shonk (2008).

4.1 Horizontal cloud inhomogeneity

There have been numerous studies in the literature that have used different observational datasets to quantify the degree of inhomogeneity that is found in different types of cloud. In this section we compare them. The first task is to convert the various measures of inhomogeneity into a common metric. We use the fractional standard deviation of in-cloud water content, defined simply as $f_w = \sigma_w / \bar{w}$, where \bar{w} is the mean water content (or its vertical integral, the water path, in some studies) and σ_w is the standard deviation of water content. Note that for small values of f_w , we find that $f_w \approx \sigma_{\ln w}$. If particle size is assumed constant then f_w will be equal to the fractional standard deviation of extinction coefficient, or its vertical integral, optical depth. Clear-sky regions are not considered in the calculation in any of the studies. Hogan and Illingworth (2003) used the fractional variance, which is simply f_w^2 , while Barker et al. (1996) used a parameter $\nu = f_w^{-2}$.

The resulting values of f_w are shown in Fig. 5. Since each study considered a different averaging area, which we might expect to be important, the results are plotted against the equivalent model gridbox size. Most studies produced a single value for each cloud type, although Hogan and Illingworth (2003) reported a gridbox-size-dependent relationship that is depicted by the blue diagonal line. The results are colour-coded according to the observational method used. The blue and black points indicate radar and aircraft measurements, respectively, which are measures of fractional standard deviation at a particular height in the cloud. By contrast, the red and cyan points are measurements by passive satellite and ground-based microwave radiometers, which are measures of the fractional standard deviation of the vertical integral of water content (or more exactly in the case of satellite measurements, of the optical depth). We might expect vertical integrals to have a lower fractional standard deviation, since they average structures at different levels that may be uncorrelated, but there is little sign of systematically lower values for these points. One possible consideration is that optical measurements are sensitive to a lower moment of the size distribution than radar measurements, and it may be that these moments have a different fractional standard deviation.

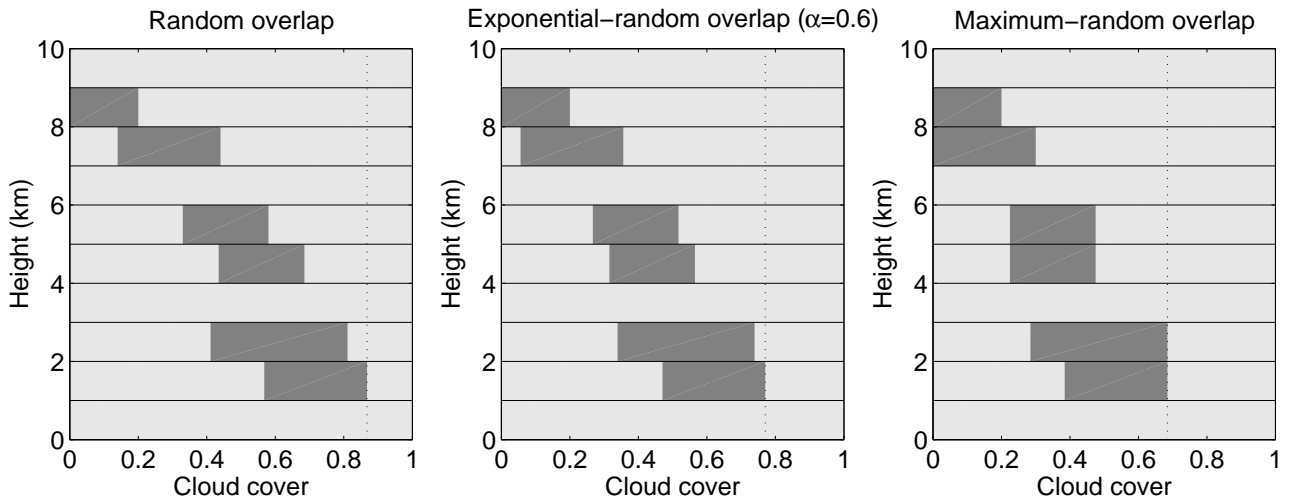


Figure 6: Schematic of three possible cloud overlap assumptions in the columns of a GCM, with the vertical dotted line showing the total column cloud cover. All assume that clouds in layers with a cloud-free layer between them are randomly overlapped, but the assumption of the overlap of clouds in adjacent layers varies from random on the left to maximum on the right. The central panel shows the use of an overlap parameter α (in this case with a value of 0.6 between all adjacent levels) describing the overlap relative to random ($\alpha = 0$) and maximum ($\alpha = 1$).

The spread of points shows no dependence on the size of the gridbox, despite the fact that in individual studies a dependence is found due to the fact that increasing the size of the gridbox means that larger scales of variability are included (e.g. Hogan and Illingworth 2003). Presumably the spread caused by other factors means that the dependence on gridbox size is obscured. Note that the study of Cahalan et al. (1994) has a large equivalent gridbox size because it was from of order a month of continuous observations.

The greatest surprise is the lack of a strong dependence on cloud type. Visually, cirrus clouds have a more homogeneous appearance than stratocumulus, and yet there is no real evidence in Fig. 5 that they have a smaller f_w . This is likely to be because ice clouds have variability on larger scales than liquid clouds, so while they lack the small scale structure that is apparent from the ground, when we consider all scales within a GCM gridbox the two cloud types are comparable. One exception to this rule is cumulus, which Barker et al. (1996) showed to have a significantly greater variability than stratocumulus. This result was also reported by Pincus et al. (1999) who examined a range of boundary-layer cloud types. We should be wary of the exact f_w shown for cumulus in Fig. 5, however, since cumulus clouds are most susceptible to 3D effects in optical depth retrievals. Given these results, it may be justified to use a single value for f_w globally, but there is clearly more work to be done to reconcile the effects of different observing systems, for example by calculating f_w simultaneously from the same cloud using different methods.

4.2 Cloud overlap

The importance of cloud overlap is illustrated in Fig. 6, which shows three idealized model columns, each with the same profile of cloud fraction. However, the different assumptions on the way the clouds in each level are overlapped lead to a significantly different total cloud “cover” (the fractional area of cloud projected on to the ground). It was shown by Morcrette and Jakob (2000) that this leads to significantly different planetary albedo. The random overlap assumption assumes that clouds in all levels are randomly overlapped with respect to each other, but has the unphysical property that the total cloud cover increases significantly as the vertical resolution of the model improves (although all assumptions have some sensitivity to vertical resolution). Most models currently use the “maximum-random” overlap assumption, meaning that cloud in adjacent levels is overlapped to the maximum extent, while clouds that are separated by cloud-free levels are randomly overlapped. In order

to test this we can use cloud radar data of the type shown in Fig. 4, and careful inspection of panel b of this figure reveals that clouds in adjacent levels are often somewhere between the two extremes of maximum and random overlap, as illustrated by the middle panel of Fig. 6.

Hogan and Illingworth (2000) quantified this behaviour as follows. Suppose we consider two levels of the atmosphere, which may or may not be adjacent, and which have a cloud fraction of c_a and c_b . If they were randomly overlapped, then the combined cloud cover of these two levels *excluding any levels in between* would be $C_{\text{rand}} = c_a + c_b - c_a c_b$, while assuming maximum overlap would be $C_{\text{max}} = \max(c_a, c_b)$. Radar observations can also provide us with the “true” combined cloud cover, C_{true} . Analysis of a large volume of data allows the mean of these different values of C to be calculated as a function of the distance between levels, and whether there is any intervening cloud between the levels under consideration. Hogan and Illingworth (2000) then introduced an “overlap parameter”, defined as

$$\alpha = \frac{\overline{C}_{\text{true}} - \overline{C}_{\text{rand}}}{\overline{C}_{\text{max}} - \overline{C}_{\text{rand}}}, \quad (17)$$

which varies between the extremes of $\alpha = 1$ for maximum overlap to $\alpha = 0$ for random overlap (on average). The radar observations clearly showed that for clouds with clear sky between them, the overlap was random on average, as represented by all the idealizations in Fig. 6. For clouds in adjacent levels, or for pairs of levels with some cloud at all levels between them, the dependence of overlap parameter with level separation z was well fitted by an inverse exponential of the form

$$\alpha(z) = \exp(-z/z_0), \quad (18)$$

where z_0 can be thought of as an overlap “decorrelation length”.

An important point to note is that many radiation schemes that are equipped to take overlap information as input, including Tripleclouds, can only allow the overlap of adjacent layers to be specified. This can easily be seen from the discussion in section 3.4 where the overlap coefficients U and V are only specified between levels. Hence, the observed behaviour of overlap becoming more and more decorrelated with increased separation can be thought of as arising naturally from the cumulative effect of small decorrelations between adjacent levels. Therefore, for the analysis that follows we calculate z_0 from clouds in levels only 1 km apart, with the understanding that a radiation scheme would implement this by using (18) to calculate α for the particular separation of adjacent levels, and from that the values of the overlap coefficients U and V .

Values of z_0 have been derived at Chilbolton, southern England, by Hogan and Illingworth (2000), and also at the various Atmospheric Radiation Measurement sites worldwide by Mace and Benson-Troth (2002), and are shown versus absolute latitude in Fig. 7. Results from CloudSat appear to indicate a larger decorrelation length, although this is believed to be due to the fact that rain was included in the statistics, which tends to be more maximally overlapped due to the much larger fall speed. The ground-based points can be fitted by a line of the form

$$z_0 = 2.9 - 0.027|\phi|, \quad (19)$$

where z_0 is in km and ϕ is latitude in degrees. This shows a clear tendency for more maximally overlapped clouds in the tropics, presumably due to the greater prevalence of convective over stratiform clouds, and the lower wind shear. However, we stress that a simple linear fit is somewhat crude given that only four points are present, and it would be desirable to include a more physical dependence on cloud type rather than simply on latitude. Indeed, the large error bar at the Southern Great Plains ARM site indicates the range in different seasons, from the convection-dominated summer to the stratiform-dominated winter. Attempts to build in a dependence on wind shear were presented by Naud et al. (2008). It has also been shown that cloud phase has a role to play. Brooks (2005) used the radar and lidar signals at Chilbolton to distinguish between liquid and ice clouds, and found that for a model with a horizontal resolution of Δx and a vertical resolution of Δz (both in metres), the overlap parameters for adjacent levels were best fitted for liquid and ice by

$$\alpha_{\text{liquid}}(\Delta z) = 1 - 0.0097\Delta x^{-0.0214}\Delta z^{0.6461}; \quad \alpha_{\text{ice}}(\Delta z) = 1 - 0.0115\Delta x^{-0.0728}\Delta z^{0.5903}. \quad (20)$$

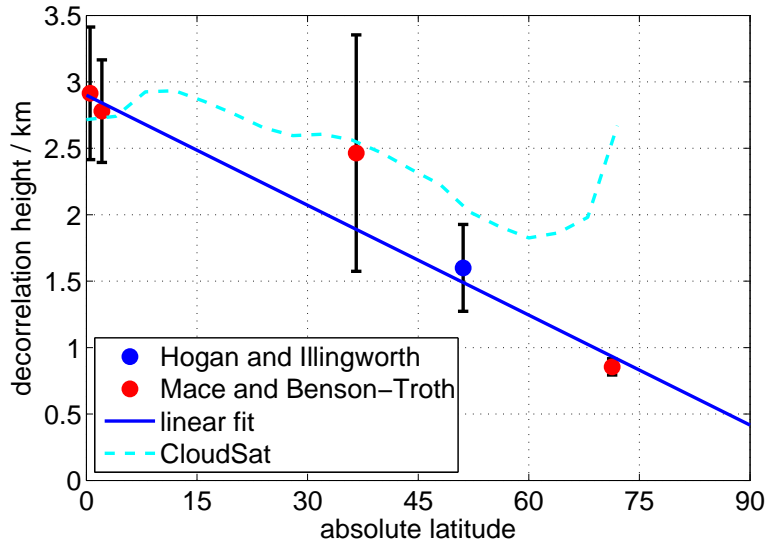


Figure 7: Estimate of the variation of overlap decorrelation height, z_0 in (18), versus absolute latitude, for vertically continuous cloud. The ground-based observations were from Chilbolton (Hogan and Illingworth 2000), with the error bar indicating the dependence on gridbox size, and the various permanent ARM sites globally (Mace and Benson-Troth 2002), with the error bars indicating the seasonal variation at each site. The cyan dashed line was calculated from spaceborne CloudSat radar and CALIPSO lidar data (G. G. Mace, personal communication), but includes rain. The blue line provides a linear fit to the ground-based data points. Adapted from Shonk (2008).

For typical model resolutions it was found that liquid clouds tended to be more randomly overlapped than ice clouds. A possible reason for this is that liquid clouds often occur in the form of thin layers, and when observations are discretized to the finite vertical resolution of a model, physically separate layers can occur in adjacent model levels. By contrast, ice clouds are deeper and ice particles fall at around 1 m s^{-1} , leading to a greater correlation of cloud occurrence between levels.

4.3 Overlap of cloud inhomogeneities

The previous section discussed the overlap of cloud boundaries, but an additional consideration for radiative transfer is the degree to which in-cloud inhomogeneities in water content are overlapped in the vertical. The only study in which this has been calculated from observations was by Hogan and Illingworth (2003), who used cloud radar to quantify the vertical correlation of horizontal inhomogeneities in cirrus clouds. They found that the decorrelation length for inhomogeneities increased with horizontal gridbox size, but decreased with increased wind shear. Generally their values were less than 1 km, which is substantially less than the values found for the overlap of cloud boundaries in the previous section. Hogan and Kew (2005) calculated that the top-of-atmosphere effect of different cirrus fallstreaks orientations in response to changed wind shear could be of order 20 W m^{-2} in the shortwave and 10 W m^{-2} in the longwave.

Unfortunately it is much more difficult to estimate the overlap of inhomogeneities in stratocumulus clouds, since most such clouds contain radiatively unimportant drizzle drops that dominate the radar return, and hence the vertical distribution of water content cannot be reliably derived. Given these issues, a number of implementations of McICA simply assume that the decorrelation length for cloud inhomogeneities is half the decorrelation length for cloud boundaries (e.g. Morcrette et al. 2008), although it would clearly be desirable to put this figure on a firmer observational footing.

5 The global impact of cloud inhomogeneity and overlap

In this section we estimate the global impact of cloud inhomogeneity and overlap, and hence the likely errors that are present in current climate models that assume clouds to be horizontally homogeneous within the cloudy fraction of the gridbox, and overlapped according to the rules of maximum-random overlap. We take a month of global ERA-40 model fields from each of the four seasons in the year 2001, including cloud fraction, liquid water content and ice water content. Four off-line experiments are performed using the Edwards-Slingo radiation code:

1. Using the common assumptions of horizontally homogeneous (plane-parallel) clouds and maximum-random overlap.
2. Using horizontally homogeneous clouds, but with more realistic “exponential-random” overlap, in which the overlap parameter varies with latitude according to the fit shown in Fig. 7. In fact a pressure-dependent correlation length is used, because this produces better agreement with the finding of Brooks (2005) that low liquid clouds are more randomly overlapped than high ice clouds (evident from plugging typical numbers into Eq. 20).
3. Using maximum-random overlap, but with the “Tripleclouds” scheme to represent inhomogeneity with a fractional standard deviation of $f_w = 0.8$ for all cloud types (a reasonable average of the studies summarized in Fig. 5). This is achieved by setting the water content values in the two cloudy regions to $w = \bar{w} \pm f_w$, where \bar{w} is the mean water content provided by the ERA-40 data.
4. Using both exponential-random overlap and Tripleclouds, thereby correcting both of the main biases relating to cloud structure that are present in current climate models. In this case, the overlap decorrelation length of the cloud inhomogeneities is assumed to be $2/3$ of the value for the cloud boundaries.

Additionally, we perform a calculation using the same model state but with no clouds present, in order that the cloud radiative forcing (CRF) of all the previous runs may be calculated. CRF is defined as the top-of-atmosphere net shortwave or longwave radiation (downwelling minus upwelling) of the cloudy case minus that of the clear-sky case.

The results are shown in Fig. 8 versus latitude for the shortwave, longwave and net (the sum of the two). The dark blue line shows the results for Experiment 1 above, in which clouds are represented as in most current climate models. As in previous studies, this shows shortwave CRF to be negative, indicating that the high solar albedo of clouds is in the sense of a cooling effect on climate, while longwave CRF is positive, indicating that clouds act to warm the climate in this part of the spectrum in a similar way to greenhouse gases. In a global average the shortwave effect is dominant and the net CRF is negative.

The light blue line in Fig. 8 shows the results of Experiment 2 in which more realistic overlap is used but the clouds are still horizontally homogeneous in each model level. It can be seen that the magnitude of the CRF is increased in both the longwave and the shortwave due to the fact that the global cloud cover has been increased. The red line shows the effect of representing cloud inhomogeneity (Experiment 3) but retaining maximum-random overlap. This time the CRF is reduced by an amount that is significantly larger than the effect of using more realistic overlap. Finally, the black line shows Experiment 4 in which both cloud inhomogeneity and realistic overlap are used, which reveals a significant net reduction in CRF compared with Experiment 1, but not by as much as Experiment 3.

Hence we conclude that it is important to represent both the effects of both realistic overlap and cloud inhomogeneity in order for the radiative effects of clouds to be accurately captured. If only the overlap representation is improved then the CRF will actually be less accurate, while if only the effects of cloud inhomogeneity are introduced then the result will be an overcompensation for the CRF error. This point was also made by Hogan and Kew (2005) for individual cirrus clouds.

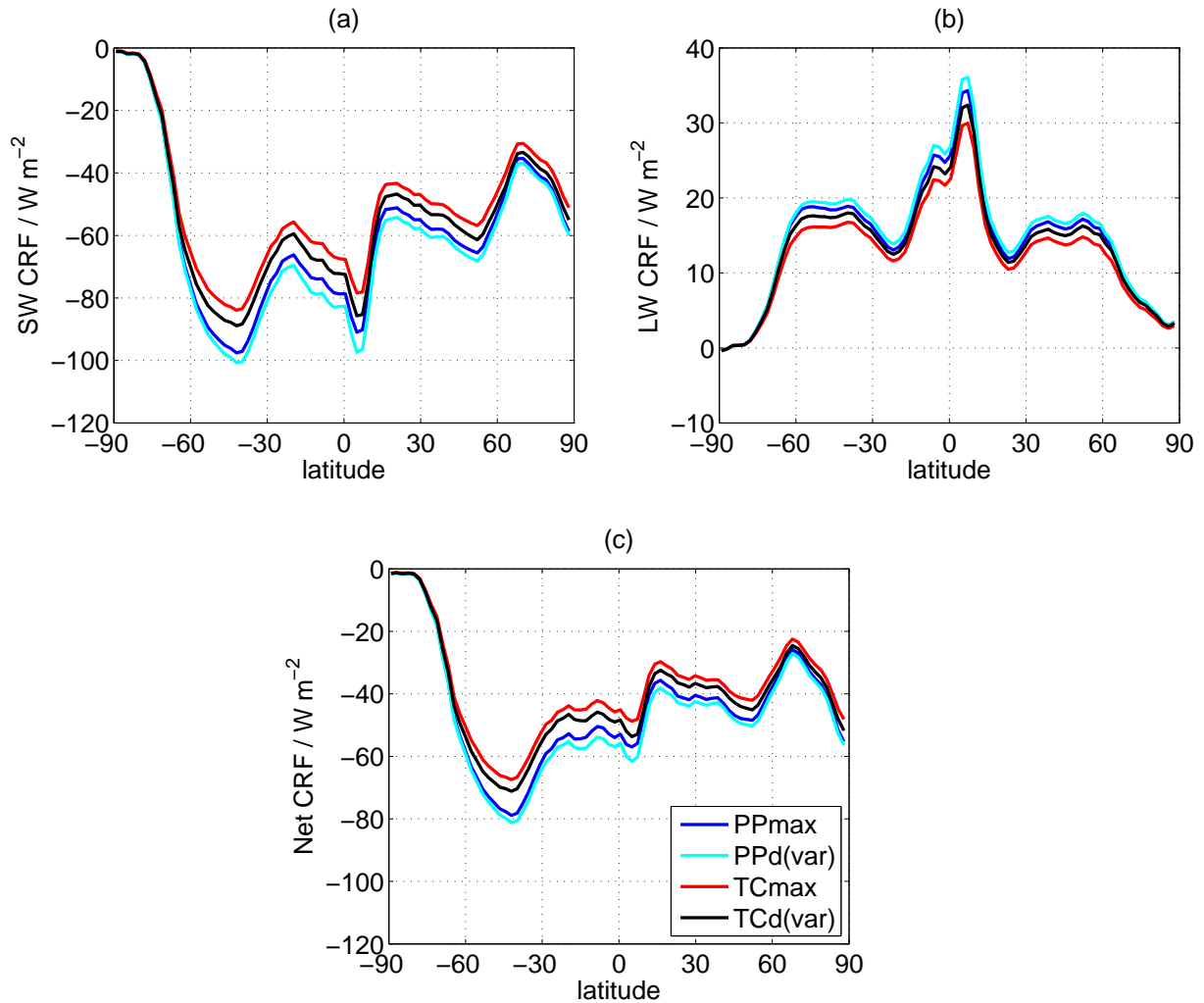


Figure 8: Top-of-atmosphere cloud radiative forcing in the (a) shortwave, (b) longwave and (c) net, for four experiments performed on a selection of ERA-40 data. The order of the colours in the legend corresponds to experiments 1–4 described in section 5. From Shonk (2008).

The longitudinally averaged changes to CRF hide significant regional variations due to the different behaviours of different types of cloud. Figure 9 shows the global distribution of the changes to CRF when the representation of both overlap and inhomogeneity is improved. In the stratocumulus regions on the eastern sides of ocean basins, the clouds tend to be physically thin and fill the gridbox horizontally, resulting in the inhomogeneity effect dominating over the overlap effect. Since the shortwave effect of these clouds is much larger than the longwave effect, the net CRF is increased (becomes less negative) in these regions by up to around 15 W m^{-2} (around 20%). In the convective region of the tropical West Pacific, most clouds only partially fill the gridbox yet occupy many vertical levels. Hence in the shortwave the overlap effect almost completely counteracts the inhomogeneity effect and the change is only around 4 W m^{-2} . In the longwave, the overlap effect in this region dominates and the change in CRF is around -4 W m^{-2} , resulting in a near cancellation in the net. In the mid-latitude storm-track regions, both effects are important in both the shortwave and longwave, but with the shortwave effect of the inhomogeneity having the upper hand, resulting in a net increase of CRF (i.e. becoming less negative). Further analysis of these runs was presented by Shonk (2008).

As a final point we note that these results are subject to the accuracy of the clouds in the ERA-40 analysis, and some appreciable errors have been revealed in previous studies (e.g. Allan and Ringer 2003). These could be expected to change the precise values shown here, although the broad patterns are believed to be robust.

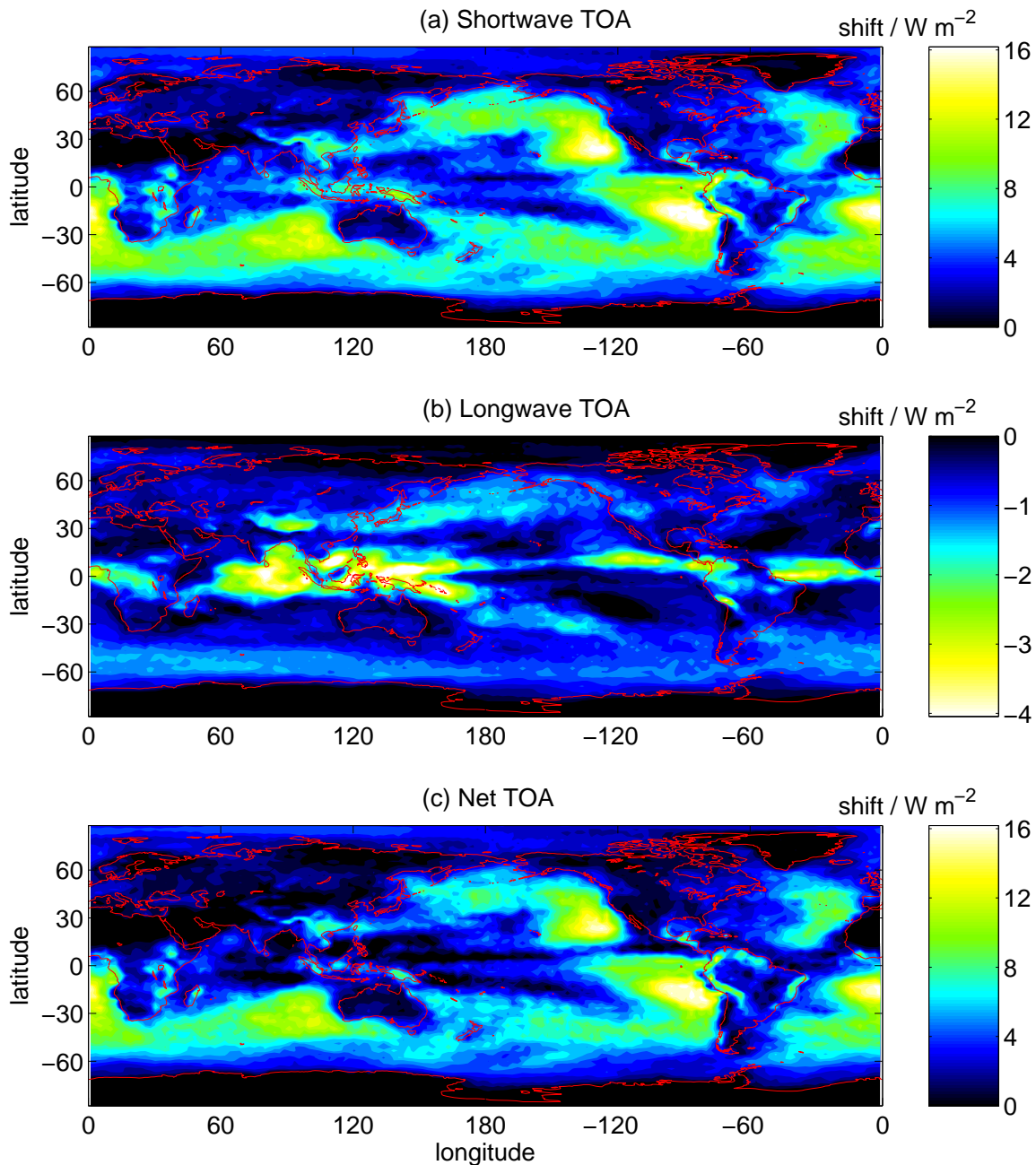


Figure 9: The change in top-of-atmosphere cloud radiative forcing in the (a) shortwave, (b) longwave and (c) net, when improving both the representations of cloud overlap and inhomogeneity in a radiation scheme (i.e. Expt. 4 minus Expt. 1). Note that since shortwave CRF is negative, a positive change in panel a indicates a reduction in the magnitude of the shortwave CRF. Adapted from Shonk (2008).

6 Three-dimensional radiative transfer

So far we have treated the ICA as “truth” against which to test more efficient methods for representing cloud structure, such as McICA and Tripleclouds. As the name implies, the ICA is an approximation, but how good an approximation is it? We can imagine radiation entering or leaving the edges of clouds, which do not exist in the ICA, but often there is a significant degree of cancellation between a net gain of radiation into a cloud side in one part of the domain and a net loss out of a cloud side elsewhere. To explain how 3D effects can change domain-averaged fluxes and heating rates, it is convenient to simplify the multitude of ways that radiation can interact

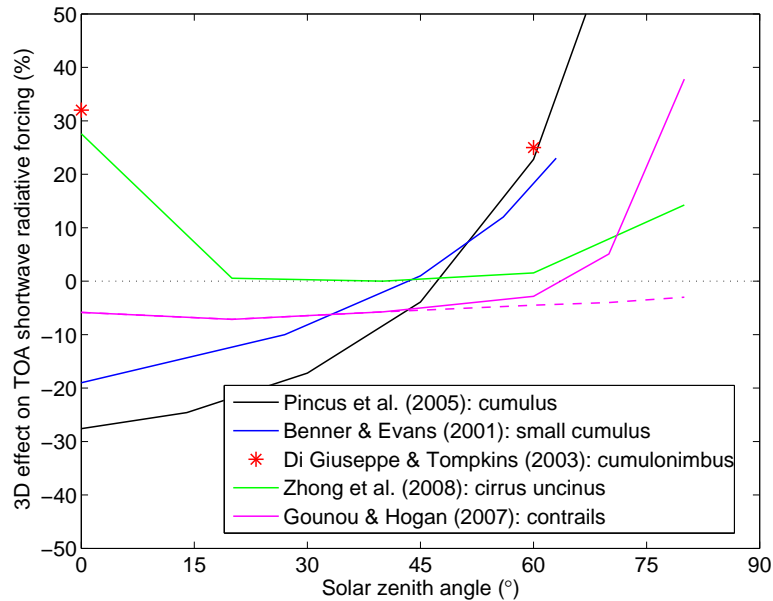


Figure 10: Effect on shortwave top-of-atmosphere cloud radiative forcing of 3D radiative transport (compared to an ICA calculation) for several different cloud types. The solid magenta line shows the results for a contrail of optical depth 0.4 illuminated perpendicular to its length, while the dashed magenta line is for illumination parallel to its length. The cirrus uncinus case had a domain-mean optical depth of 1.2.

with a complex cloud field into three dominant processes. These were described by Gounou and Hogan (2007) for the simple geometrical structure of an aircraft contrail (where 3D effects turn out to be very significant), but essentially the same mechanisms have been outlined by Várnai and Davies (1999) in the shortwave and Killen and Ellingson (1994) in the longwave:

1. *Shortwave side illumination.* When the sun is low in the sky, the presence of cloud sides means that the incoming radiation has a greater chance to intercept a cloud than when the sun is overhead. Therefore more radiation will be scattered back to space, increasing the cloud radiative forcing. The geometrical reason behind this also explains why a field of cumulus clouds appears to cover a greater fraction of the sky when looking towards the horizon than when looking upwards.
2. *Shortwave side leakage.* When the sun is high in the sky, an opposing effect often occurs: radiation entering the cloud near the top is scattered into the forward hemisphere and has a chance of leaking out of the edge of the cloud and continuing to the ground (giving the cloud a silver lining to a ground observer). In the ICA this would not happen: this radiation would remain within the cloud and have a greater chance to be subsequently scattered back out to space. The 3D effect is therefore typically to reduce the radiative forcing.
3. *Longwave side effects.* Imagine a field of cumulus clouds that has an areal coverage of one half. For the same geometrical reason as outlined in mechanism 1, the *angular* coverage of the sky by clouds, as seen by a pyrgeometer above or below the cloud will be more than one half, on average. Because clouds tend to be colder than the surface, there will be a lower emission to space and a larger emission towards the ground, so the longwave cloud forcing at the top-of-atmosphere and at the surface is larger if 3D effects are included.

So which of these effects dominates in real clouds? Figure 10 depicts the fractional change to shortwave cloud radiative forcing, i.e. $(CRF_{3D} - CRF_{ICA})/CRF_{ICA}$, calculated for a number of different cloud types. The magnitude of the 3D effect is substantial for cumulus clouds due to their relatively large area of cloud “side”.

For large solar zenith angles θ , the side illumination effect dominates and CRF is increased, while for $\theta < 45^\circ$, the side leakage effect dominates and CRF is reduced. Cirrus clouds and contrails exhibit approximately the same behaviour, but presumably because their thickness-to-width ratio is lower, the transition occurs at a larger value of θ . The dashed line shows that for contrails, the side illumination effect can be removed completely by orienting the contrail parallel to the direction of the incoming sun. For cumulonimbus, the results for $\theta = 60^\circ$ are close to the results for cumulus clouds, but for $\theta = 0^\circ$, the behaviour is quite different. A possible explanation is the role of absorption in deep clouds: Di Giuseppe and Tompkins (2003) showed that for overhead sun the domain-mean absorption was reduced in the 3D calculation, suggesting that photons that leaked from cloud sides had a higher probability of escaping back to space than the equivalent photons in the ICA that stayed within the cloud and were more likely to be absorbed. However, it remains a puzzle to explain the similar behaviour reported by Zhong et al. (2008) for thin cirrus clouds (the leftmost point of the green line in Fig. 10). Stratiform clouds, such as stratocumulus (Zuidema and Evans 1998) and optically thicker cirrus (Zhong et al. 2008) exhibit much weaker 3D effects in the shortwave, typically at the 2% level, so have not been shown in Fig. 10.

There have been fewer studies of the longwave 3D effect for realistic cloud fields. It was found by Gounou and Hogan (2007) and Zhong et al. (2008) that the top-of-atmosphere longwave CRF was enhanced by around 10% for contrails and optically thin cirrus, but for ice clouds with an optical depth larger than around 5 the effect was closer to 1%. Boundary-layer clouds generally have a much larger surface than top-of-atmosphere CRF in the longwave, and it was estimated by Heidinger and Cox (1996) that cumulus clouds increase the surface longwave forcing by as much as 30%.

The ultimate aim is to find a way to represent these effects efficiently in a GCM radiation scheme. In terms of the part of the code requiring modification, the three mechanisms listed above will specifically affect (1) the direct incoming shortwave calculation, (2) the diffuse shortwave calculation, and (3) the diffuse longwave calculation. Tompkins and Di Giuseppe (2007) tackled mechanism 1 by making the overlap assumption in the shortwave dependent on the solar zenith angle, thereby accounting for the fact that when the sun is close to the horizon the incoming sunlight is more likely to intercept a cloud. To fully simulate 3D effects it will be necessary to also represent mechanisms 2 and 3, which could involve changes to the way the two-stream equations are solved to allow for radiation to pass horizontally through the edges of clouds, and indeed between internal inhomogeneities in the cloud. However, we should tread cautiously: although Fig. 10 shows that the instantaneous effects can be large for certain cloud types, there can be substantial cancellation between the two shortwave effects over the diurnal cycle. Moreover, it remains to be seen whether it is possible to characterize complex 3D structure by a handful of variables (such as the effective area of cloud edge within a gridbox) that could be used in a radiation scheme.

7 Conclusions and outlook

In this article we have shown that the two leading sources of error in the sub-grid representation of clouds in radiation schemes, namely cloud inhomogeneity and cloud overlap, may now be represented efficiently in GCMs. Indeed, there are at least two viable algorithms, McICA (Pincus et al. 2003) and Tripleclouds (Shonk and Hogan 2008). Using Tripleclouds, we have estimated the global impact of these two effects on the radiation budget, and hence the errors that are likely to be present in climate models. Naturally there will be a dynamical response to changes to the global distribution of incoming radiation, and work is currently underway to implement Tripleclouds in the Met Office climate model to quantify it. The intention is also to make use of the inhomogeneity information available from the new ‘‘PC2’’ cloud scheme (Wilson et al. 2008), rather than relying on empirical relationships.

There are numerous other possible sources of error and inconsistency in the way that clouds are treated in radiation schemes, and which deserve further attention. Three-dimensional effects were discussed in the previous section, and if a way can be found to represent them efficiently then more information will be required from

observations on the typical area of “cloud edge” within a model gridbox. More generally, it would be desirable to synthesize cloud observations into an overarching “theory of cloud structure” (no doubt based on fractal principles) that enables the various quantities required by a radiation scheme to be predicted in a way that is intrinsically dependent on gridbox size and all the other relevant variables, rather than relying on crude empirical relationships that obscure the underlying physics. Including gridbox-size-dependent parametrizations is important for a number of models that are run routinely at a wide range of resolutions, yet most fail to include it rigorously. Improvements along these lines could be extended to include the fact that individual cloud realizations do not always exhibit mean inhomogeneity and mean overlap behaviour, but rather can take on a range of values. Perhaps it is important to include a stochastic element to represent the known fluctuations of these properties from case to case.

It is worth pointing out that the innovations in representing the interactions of clouds with radiation may also be useful for other parts of the GCM, specifically aspects of the microphysics such as precipitation formation. It was shown by Jakob and Klein (2000) that cloud overlap affects the fraction of precipitation reaches the ground without evaporating. Is there a way that overlap, inhomogeneity and particle size information can be made to be consistent between the various schemes?

So far we have discussed only the accuracy of a radiation scheme given the inputs from the GCM. However, the most substantial source of error in calculating the radiative properties of clouds is almost certainly due to errors in the cloud variables themselves. For example, when the radiation budget of ERA-40 is compared to CERES observations, there is a distinct underestimate of convection over the Amazon, and an underestimate of the longwave CRF in mid-latitudes that is larger than the differences between the various combinations of cloud inhomogeneity and overlap discussed in section 5. Therefore the greatest challenge is to make use of ground-based and spaceborne observations, coupled with analysis techniques such as those of Illingworth et al. (2007), to identify specific errors in the way clouds are represented and remedy them with better cloud parametrizations.

Acknowledgements. The development of “Tripleclouds” would not have been possible without the ingenious and meticulous coding of John Edwards in the relevant subroutines of the Edwards-Slingo code. Robert Pincus is thanked for valuable comments on a draft of the article. Francesca Di Giuseppe, Wenyi Zhong and Robert Pincus are thanked for providing the necessary information to enable their papers to be compared in Fig. 10.

References

- Allan, R. P. and M. A. Ringer, 2003: Inconsistencies between satellite estimates of long-wave cloud radiative forcing and dynamical fields from re-analyses. *Geophys. Res. Lett.*, **30**, doi:10.1029/2003GL017019.
- Barker, H. W., B. A. Wielicki and L. Parker, 1996: A parametrization for computing grid-averaged solar fluxes for inhomogeneous marine boundary layer clouds - 2. Validation using satellite data. *J. Atmos. Sci.*, **53**, 2304–2316.
- Brooks, M. E., 2005: *Clouds and radiation: Using radar/lidar synergy to evaluate and improve models*. PhD thesis, University of Reading.
- Cahalan, R. F., W. Ridgway, W. J. Wiscombe, T. L. Bell and J. B. Snyder, 1994: The albedo of fractal stratocumulus clouds. *J. Atmos. Sci.*, **51**, 2434–2455.
- Chandrasekhar, S., 1950: *Radiative Transfer*. Dover, New York.
- Di Giuseppe, F., and A. M. Tompkins, 2003: Three-dimensional radiative transfer in tropical deep convective clouds. *J. Geophys. Res.*, **108**, doi:10.1029/2003JD003392.
- Edwards, J., and A. Slingo, 1996: Studies with a flexible new radiation code - 1. Choosing a configuration for a large-scale model. *Quart. J. Roy. Meteorol. Soc.*, **122**, 689–719.
- Evans, K. F., 1998: The spherical harmonic discrete ordinate method for three-dimensional atmospheric radiative transfer. *J. Atmos. Sci.*, **55**, 429–446.
- Feynman, R. P., R. B. Leighton and M. Sands, 1964: *The Feynman lectures on physics - 2. Mainly electromagnetism and matter*. Addison-Wesley.
- Fu, Q., K. N. Liou, M. C. Cribb, T. P. Charlock and A. Grossman, 1997: Multiple scattering parameterization in thermal infrared radiative transfer. *J. Atmos. Sci.*, **54**, 2799–2812.

- Giovanelli, R. G., 1959: Radiative transfer in non-uniform media. *Aust. J. Phys.*, **12**, 164–170.
- Gounou, A., and R. J. Hogan, 2007: A sensitivity study of the effect of horizontal photon transport on the radiative forcing of contrails. *J. Atmos. Sci.*, **64**, 1706–1716.
- Heidinger, A. K., and S. K. Cox, 1996: Finite-cloud effects in longwave radiative transfer. *J. Atmos. Sci.*, **53**, 953–963.
- Hogan, R. J., and A. Battaglia, 2008: Fast lidar and radar multiple-scattering models - 2. Wide-angle scattering using the time-dependent two-stream approximation. *J. Atmos. Sci.*, **65**, 3636–3651.
- Hogan, R. J. and A. J. Illingworth, 2000: Deriving cloud overlap statistics from radar. *Quart. J. Roy. Meteorol. Soc.*, **126**, 2903–2909.
- Hogan, R. J. and A. J. Illingworth, 2003: Parametrising ice cloud inhomogeneity and the overlap of inhomogeneities using cloud radar data. *J. Atmos. Sci.*, **60**, 756–767.
- Hogan, R. J. and S. F. Kew, 2005: A 3D stochastic cloud model for investigating the radiative properties of inhomogeneous cirrus clouds. *Quart. J. Roy. Meteorol. Soc.*, **131**, 2585–2608.
- Huygens, C, 1690: *Treatise on light*. Trans., S. P. Tompson, 1912, Chicago: <http://www.gutenberg.org/etext/14725>.
- Iacono, M. J., E. J. Mlawer, S. A. Clough and J.-J. Morcrette, 2000: Impact of an improved longwave radiation model, RRTM, on the energy budget and thermodynamic properties of the NCAR community climate model, CCM3. *J. Geophys. Res.*, **105**, 14873–14890.
- Ibn al-Haytham, A. (Alhacen), 1021: *The Book of Optics*. Available as “Alhacen’s theory of visual perception”, Ed. & Trans., M. A. Smith, 2001, *Trans. Am. Phil. Soc.*, **91**.
- Illingworth, A. J., R. J. Hogan, E. J. O’Connor, D. Bouniol, M. E. Brooks, J. Delanoe, D. P. Donovan, J. D. Eastment, N. Gaussiat, J. W. F. Goddard, M. Haeffelin, H. Klein Baltink, O. A. Krasnov, J. Pelon, J.-M. Piriou, A. Protat, H. W. J. Russchenberg, A. Seifert, A. M. Tompkins, G.-J. van Zadelhoff, F. Vinit, U. Willen, D. R. Wilson and C. L. Wrench, 2007: Cloudnet—continuous evaluation of cloud profiles in seven operational models using ground-based observations. *Bull. Am. Meteorol. Soc.*, **88**, 883–898.
- Jakob, C., and S. X. Klein, 2001: A parametrization of the effects of cloud and precipitation overlap for use in general-circulation models. *Quart. J. Roy. Meteorol. Soc.*, **126**, 2525–2544.
- Killen, R. M., and R. G. Ellingson, 1994: The effect of shape and spatial distribution of cumulus clouds on longwave irradiance. *J. Atmos. Sci.*, **51**, 2123–2136.
- Lacis, A., and V. Oinas, 1991: A description of the correlated *k*-distribution method for modeling nongray gaseous absorption, thermal emission, and multiple scattering in vertically inhomogeneous atmospheres. *J. Geophys. Res.*, **96**, 9027–9063.
- Li, J., and H. W. Barker, 2005: A radiation algorithm with correlated-k distribution - 1. Local thermal equilibrium. *J. Atmos. Sci.*, **62**, 286–309.
- Liu, Q., and F. Weng, 2002: A microwave polarimetric two-stream radiative transfer model. *J. Atmos. Sci.*, **59**, 2396–2402.
- Mace, G. G. and S. Benson-Troth, 2002: Cloud-layer overlap characteristics derived from long-term cloud radar data. *J. Clim.*, **15**, 2505–2515.
- Maxwell, J. C., 1873: *A treatise on electricity and magnetism*. Clarendon Press, Oxford.
- Meador, W. E. and W. R. Weaver, 1980: Two-stream approximations to radiative transfer in planetary atmospheres: a unified description of existing methods and a new improvement. *J. Atmos. Sci.*, **37**, 630–643.
- Mie, G., 1908: Beiträge zur Optik trüber Medien, speziell kolloidaler Metallösungen. *Ann. Phys.* **330**, 377-445.
- Mishchenko, M. I., 2002: Vector radiative transfer equation for arbitrarily shaped and arbitrarily oriented particles: a microphysical derivation from statistical electromagnetics. *Appl. Opt.*, **41**, 7114–7135.
- Mishchenko, M. I., J. W. Hovenier and L. D. Travis, 2000: *Light scattering by nonspherical particles*. Academic Press.
- Mishchenko, M. I., L. D. Travis, and A. A. Lacis, 2006: *Multiple scattering of light by particles: radiative transfer and coherent backscattering*. Cambridge.
- Mlawer, E. J., S. J. Taubman, P. D. Brown, M. J. Clough and A. Shepard, 1996: Radiative transfer for inhomogeneous atmospheres: RRTM, a validated correlated-k model for the longwave. *J. Geophys. Res.*, **102**, 16663–16682.
- Morcrette, J.-J., 2000: On the effects of the temporal and spatial sampling of radiation fields on the ECMWF forecasts and analyses. *Mon. Weath. Rev.*, **128**, 876–887.
- Morcrette, J.-J., and C. Jakob, 2000: The response of the ECMWF model to changes in the cloud overlap assumption. *Mon. Weath. Rev.*, **128**, 1707–1732.

- Morcrette, J.-J., H. W. Barker, J. N. S. Cole, M. J. Iacono and R. Pincus, 2008: Impact of a new radiation package, McRad, in the ECMWF Integrated Forecasting System. *Mon. Weath. Rev.*, in press.
- Naud, C. M., A. DelGenio, G. G. Mace, S. Benson, E. E. Clothiaux and P. Kollias, 2008: Impact of dynamics and atmospheric state on cloud vertical overlap. *J. Clim.*, **21**, 1758-1770.
- Newton, I., 1704: *Opticks: or, a treatise of the reflections, refractions, inflections and colours of light*. Available from <http://www.rarebookroom.org/Control/nwtopt/>.
- Oreopoulos, L., and R. F. Cahalan, 2005: Cloud inhomogeneity from MODIS. *J. Clim.*, **18**, 5110–5124.
- Petty, G. W., 2006: *A first course in atmospheric radiation*. 2nd Ed., Sundog, Madison.
- Pincus, R., S. A. McFarlane and S. A. Klein, 1999: Albedo bias and the horizontal variability of clouds in subtropical marine boundary layers: Observations from ships and satellites. *J. Geophys. Res.*, **104**, 6183–6191.
- Pincus, R., H. W. Barker and J.-J. Morcrette, 2003: A fast, flexible, approximate technique for computing radiative transfer in inhomogeneous cloud fields. *J. Geophys. Res.*, **108**, doi:10.1029/2002JD003322.
- Pincus, R., C. Hannay and K. F. Evans, 2005: The accuracy of determining three-dimensional radiative transfer effects in cumulus clouds using ground-based profiling instruments. *J. Atmos. Sci.*, **62**, 2284–2293.
- Pomroy, H., and A. J. Illingworth, 2000: Ice cloud inhomogeneity: quantifying bias in emissivity from radar observations. *Geophys. Res. Lett.*, **27**, 2101–2104.
- Räisänen, P., H. W. Barker, M. F. Khairoutdinov, J. Li and D. A. Randall, 2004: Stochastic generation of subgrid-scale cloudy columns for large-scale models. *Quart. J. Roy. Meteorol. Soc.*, **130**, 2047–2067.
- Rossow, W. B., C. Delo and B. Cairns, 2002: Implications of the observed mesoscale variations of clouds for the Earth's radiation budget. *J. Clim.*, **15**, 557–585.
- Schuster, A., 1905: Radiation through a foggy atmosphere. *Astrophys. J.*, **21**, 1-22.
- Shonk, J. K. P., 2008: Representing horizontal and vertical cloud inhomogeneity in a one-dimensional radiation scheme, PhD thesis, University of Reading.
- Shonk, J. K. P., and R. J. Hogan, 2008: Tripleclouds: an efficient method for representing horizontal cloud inhomogeneity in 1D radiation schemes by using three regions at each height. *J. Clim.*, **21**, 2352–2370.
- Smith, S. A. and A. D. DelGenio, 2001: Analysis of aircraft, radiosonde and radar observations in cirrus clouds observed during FIRE II: The interactions between environmental structure, turbulence and cloud microphysical properties. *J. Atmos. Sci.*, **58**, 451–461.
- Stamnes, K., S. C. Tsay, W. J. Wiscombe and K. Jayaweera, 1988: Numerically stable algorithm for discrete-ordinate-method radiative transfer in multiple scattering and emitting layered media. *Appl. Opt.*, **27**, 2502–2509.
- Stephens, G. L., P. M. Gabriel and P. T. Partain, 2001: Parameterization of atmospheric radiative transfer - 1. Validity of simple models. *J. Atmos. Sci.*, **58**, 3391–3409.
- Tiedtke, M., 1996: An extension of cloud-radiation parameterization in the ECMWF model: the representation of sub-grid-scale variations of optical depth. *Mon. Weath. Rev.*, **124**, 745–750.
- Tompkins, A. M., 2002: A prognostic parameterization for the sub-grid-scale variability of water vapor and clouds in large-scale models and its use to diagnose cloud cover. *J. Atmos. Sci.*, **59**, 1917–1942.
- Tompkins, A. M., and F. Di Giuseppe, 2007: Generalising cloud overlap treatment to include solar zenith angle effects on cloud geometry. *J. Atmos. Sci.*, **64**, 2116–2125.
- Várnai, T., and R. Davies, 1999: Effects of cloud heterogeneities on shortwave radiation: Comparison of cloud-top variability and internal heterogeneity. *J. Atmos. Sci.*, **56**, 4206–4224.
- Wilson, D. R., A. C. Bushell, A. M. Kerr-Munslow, J. D. Price and C. J. Morcrette, 2008: PC2: A prognostic cloud fraction and condensation scheme - 1. Scheme description. *Quart. J. Roy. Meteorol. Soc.*, in press.
- Yang, G.-Y., and J. M. Slingo, 2001: The diurnal cycle in the tropics. *Mon. Weath. Rev.*, **129**, 784-801.
- Yang, P., and K. N. Liou, 1996: Finite-difference time domain method for light scattering by small ice crystals in three-dimensional space. *J. Opt. Soc. Am. A*, **13**, 2072–2085.
- Yee, K., 1966: Numerical solution of initial boundary value problems involving Maxwell's equations in isotropic media. *IEEE Trans. Antennas Prop.*, **14**, 302–307.
- Zhong, W., R. J. Hogan and J. D. Haigh, 2008: Three-dimensional radiative transfer in mid-latitude cirrus clouds. *Quart. J. Roy. Meteorol. Soc.*, **134**, 199–215.
- Zuidema, P., and K. F. Evans, 1998: On the validity of the independent pixel approximation for boundary layer clouds observed during ASTEX. *J. Geophys. Res.*, **103**, 6059–6074.